Letters

Coplanar Waveguide-Fed Circularly Polarized Microstrip Antenna

Chih-Yu Huang and Kin-Lu Wong

***Abstract*—Design of a square microstrip antenna for obtaining circular polarization (CP) radiation using a coplanar waveguide (CPW) feed is presented. This CP design is achieved by insetting a slit to the boundary of the square microstrip patch, which makes possible the splitting of the dominant resonant mode into two near-degenerate orthogonal modes for CP radiation and introducing an inclined slot in the CPW feed line for coupling the electromagnetic (EM) energy of the CPW to the square patch. Good impedance matching for CP operation can be obtained by adjusting the inclined slot length and the tuning-stub length of the CPW feed line. Typical experimental results are presented and discussed.**

***Index Terms*—Circular polarization, coplanar waveguides, microstrip antenna.**

I. Introduction

The coplanar waveguide (CPW)-fed microstrip antenna, similar to an aperture-coupled microstrip antenna, couples the electromagnetic (EM) energy from the feed line to the radiating patch through a coupling slot and, moreover, has a simplified structure with only two metallization levels. The microstrip antenna with a CPW feed also makes easier the integration of active devices and allows the realization of series as well as shunt connections on one side of the substrate avoiding via hole connections. Several related designs of CPW-fed microstrip antennas with different coupling slots have also been studied; such as the case with capacitively and inductively coupling slots [1]–[3] and a rectangular-ring coupling slot [4]. These designs, however, are mainly on linearly polarized radiation, and available designs for circularly polarized CPW-fed microstrip antennas are very scant in the open literature. In this letter, a circular polarization (CP) design of a CPW-fed microstrip antenna is demonstrated. A square microstrip patch with a slit [5] is used in this design and an inclined coupling slot is introduced in the CPW feed line for the excitation of the circularly polarized microstrip antenna. Details of the design considerations and experimental results are presented and discussed.

II. Antenna Design and Experimental Results

Fig. 1 shows the proposed circularly polarized microstrip antenna excited using a CPW feed line. The substrate used was a 1.6-mm-thick substrate with a dielectric constant of $\varepsilon_r = 4.4$. The CPW, designed to be with a 50-Ω characteristic impedance, has a signal strip (center conductor) of width S and a gap G between the signal strip and the coplanar ground. The 50-Ω characteristic impedance can be obtained, from simulation software Linecalc, by selecting proper values of S and G. An inclined coupling slot of length L and width G is introduced in the CPW feed line with a 45° inclination angle to the y-axis and is in parallel to the diagonal of the square radiating patch. The open-circuited stub of the CPW feed line serves as a tuning stub for fine-tuning the impedance matching of the proposed antenna. It is found that when the tuning-stub length (L_s) is adjusted to be about 0.25 wavelength of the guided wave in the substrate, good impedance matching for the proposed design can be achieved. The square radiating patch has a side length A and a narrow slit of length ℓ and width W is inserted at the boundary of the microstrip patch. Due to the slit perturbation, the equivalent excited $\hat{x}$-directed patch surface current path is lengthened, with the one in the $\hat{y}$-direction very slightly affected, which makes possible the splitting of the dominant resonant mode of the square microstrip antenna into two near-degenerate orthogonal modes for CP radiation [5]. For the proposed design shown in Fig. 1, left-hand CP radiation can be generated. Conversely, right-hand CP radiation can be obtained when the inclined coupling slot is oriented to the y-axis with a 135° inclination angle.

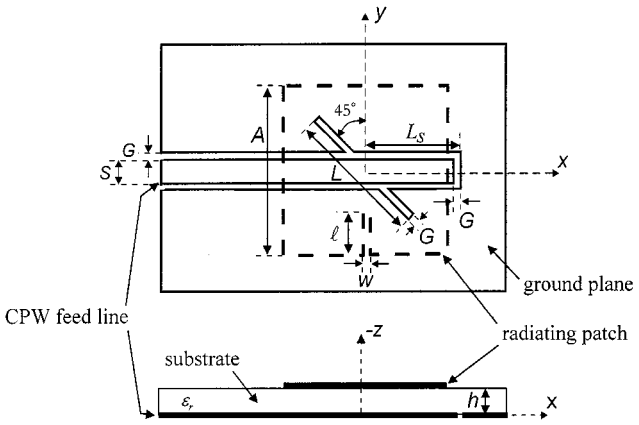

Fig. 1. Geometry of a CPW-fed circularly polarized microstrip antenna.

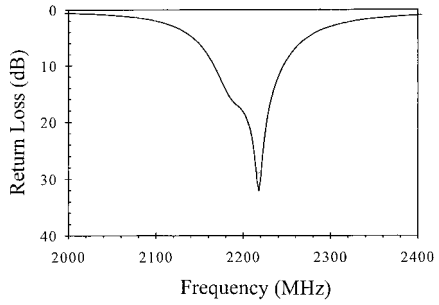

Fig. 2. Measured return loss against frequency for the proposed antenna with $\varepsilon_r = 4.4$, $h = 1.6$ mm, $S = 6.37$ mm, $G = 0.5$ mm, $L = 32$ mm, $L_s = 22$ mm, $A = 30$ mm, $\ell = 2.5$ mm, $W = 0.5$ mm, ground-plane size = 120 mm $\times$120 mm.

The proposed antenna was implemented. Typical measured return loss is shown in Fig. 2. In this case, the patch's side length was chosen to be 30 mm and the length and width of the inserted slit were 2.5 mm and 0.5 mm, respectively. The microstrip feed line was of a 50-Ω characteristic impedance and the tuning-stub length for impedance matching was adjusted to be 22 mm. From the results obtained, two near-degenerate resonant modes with good impedance matching are excited in the vicinity of the dominant resonant mode (TM_{10} or TM_{01}) of the square

Manuscript received April 12, 1999; revised November 2, 1999.

C.-Y. Huang is with the Department of Electronic Engineering, Yung Ta Institute of Technology, Pingtung, Taiwan 909, R.O.C.

K.-L. Wong is with the Department of Electrical Engineering, National Sun Yat-Sen University, Kaohsiung, Taiwan 804, R.O.C.

Publisher Item Identifier S 0018-926X(00)01655-0.

0018–926X/00$10.00 © 2000 IEEE

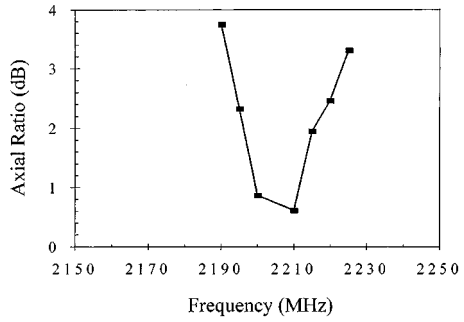

Fig. 3. Measured axial ratio in the broadside direction against frequency for the antenna shown in Fig. 2.

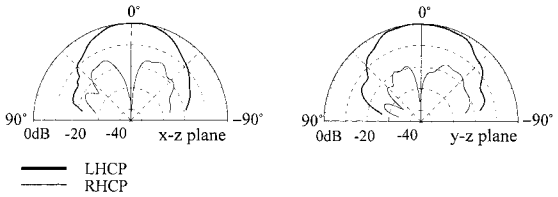

Fig. 4. Measured radiation patterns in two orthogonal planes for the antenna shown in Fig. 2 with 2206 MHz.

microstrip antenna without slit for the parameters studied here. The impedance bandwidth (10-dB return loss) is found to be 80 MHz or about 3.6% referenced to the center frequency at about 2206 MHz and, from the measured axial ratio shown in Fig. 3, the CP bandwidth, determined from 3-dB axial ratio, is found to be 36 MHz or about 1.6%. Finally, the measured radiation patterns in two orthogonal planes at 2206 MHz are also plotted in Fig. 4, and good left-hand CP radiation can be seen.

III. Conclusion

A new CP design of a CPW-fed microstrip antenna has been demonstrated. Good CP performance for the proposed antenna has also been shown. It can also be expected that by incorporating other possible microstrip patches such as a circular patch with a slit [5], a nearly square patch, a corner-truncated square patch [6], and so on, with the present proposed CPW feed with an inclined slot and an open-circuited tuning stub, CP radiation of CPW-fed microstrip antennas can be obtained.

References

[1] W. Menzel and W. Grabherr, "A microstrip patch antenna with coplanar feed line," *IEEE Microwave Guided Wave Lett.*, vol. 1, pp. 340–342, Nov. 1991.

[2] S. M. Deng, M. D. Wu, and P. Hsu, "Impedance characteristics of microstrip antennas excited by coplanar waveguides with inductive or capacitive coupling slot," *IEEE Microwave Guided Wave Lett.*, vol. 5, pp. 391–393, Nov. 1995.

[3] S. M. Deng, M. D. Wu, and P. Hsu, "Analysis of coplanar waveguide-fed microstrip antennas," *IEEE Trans. Antennas Propagat.*, vol. 43, pp. 734–737, July 1995.

[4] G. Forma and J. M. Laheurte, "CPW-fed oscillating microstrip antennas," *Electron. Lett.*, vol. 32, pp. 85–86, Jan. 1996.

[5] K. L. Wong, W. H. Hsu, and C. K. Wu, "Single-feed circularly polarized microstrip antenna with a slit," *Microwave Opt. Technol. Lett.*, vol. 18, pp. 306–308, July 1998.

[6] P. C. Sharma and K. C. Gupta, "Analysis and optimized design of single feed circularly polarized microstrip antennas," *IEEE Trans. Antennas Propagat.*, vol. 31, pp. 949–955, June 1983.

Adaptive ISAR Image Construction from Nonuniformly Undersampled Data

Yuanxun Wang and Hao Ling

***Abstract*—An adaptive approach is proposed to construct ISAR images from nonuniformly undersampled data in the angular domain. The algorithm uses an adaptive scattering feature extraction engine in place of the Fourier transform in the image construction procedure. The algorithm entails searching and extracting out individual target scattering features one at a time in an iterative fashion. The interference between different target scattering features is thus avoided and a clean ISAR image without the aliasing effect can be obtained. The algorithm is verified by constructing the ISAR image from the chamber measurement data of the model VFY-218 airplane.**

***Index Terms*—Image reconstruction, synthetic aperture radar.**

I. Introduction

Constructing an inverse synthetic aperture radar (ISAR) image of a target requires data collection in both the frequency and angular dimensions. If the data are uniformly sampled and the sampling rate is dense enough, an ISAR image can be obtained by using a two-dimensional (2-D) fast Fourier transform (FFT) algorithm [1]. In this paper, we address the case when the angular data are nonuniformly undersampled. This scenario may arise in real-world data collection when the target is fast maneuvering with respect to the radar pulse repetition interval so that the angular look on the target by the radar is not dense enough to satisfy the Nyquist sampling rate. We propose an algorithm to overcome the aliasing effect in the cross-range dimension and construct ISAR images from seriously undersampled data. The algorithm uses an adaptive scattering feature extraction engine in place of the Fourier transform in the image construction process. The original concept of adaptive feature extraction was proposed in [2] and [3]. It has been applied to ISAR image processing in the joint time–frequency space for resonant scattering mechanism extraction [4], target motion compensation [5], and Doppler interference removal [6]. In contrast to the Fourier transform, where the signal is projected to all the image-domain bases simultaneously, the adaptive algorithm searches and extracts the individual target scattering features one at a time in an iterative fashion. When applied to the present problem, the aliasing error caused by the interference between different target scattering features can be avoided. Therefore, after all the main features are extracted, they can be displayed in the ISAR image plane without the aliasing effect. We verify this algorithm by constructing the ISAR image using the chamber measurement data of the model VFY-218 airplane [7]. It is found that a reasonable ISAR image can be constructed from seriously undersampled data.

II. Adaptive Feature Extraction (AFE) Algorithm

In standard ISAR image construction, the target is assumed to be a collection of point scattering centers. Under the small-angle approx-

Manuscript received January 4, 1999; revised August 10, 1999. This work was supported by the Air Force MURI Center for Computational Electromagnetics under Contract AFOSR F49620-96-1-0025 and the Office of Naval Research under Contract N00014-98-1-0178 and N00014-98-1-0615.

The authors are with the Department of Electrical and Computer Engineering, The University of Texas at Austin, Austin, TX 78712-1084 USA.

Publisher Item Identifier S 0018-926X(00)01656-2.

0018–926X/00$10.00 © 2000 IEEE

imation, the scattered field from the target observed as a function of frequency and angle can be written as

$$E(f,\theta) = \sum_{i=1}^{N} O(x_i,y_i)e^{-2jkx_i\ \cos\theta - 2jky_i \sin\theta} \cong \sum_{i=1}^{N} O(x_i,y_i)e^{-2jkx_i - 2jk_c\theta y_i} \quad (1)$$

where $O(x_i,y_i)$ is the amplitude of the ith scattering center, k is the free-space wave number, and k_c corresponds to the wave number at the center frequency. x_i and y_i denote the down range and cross-range dimensions, respectively. We assume that the sampling in frequency is uniformly spaced and dense enough to satisfy the Nyquist criterion since it is completely controlled by the radar. Thus, the range profile versus angle data can be generated from the frequency-aspect data by applying a one-dimensional (1-D) Fourier transform along the frequency dimension. We shall denote the result as $R(x,\theta)$

$$R(x,\theta) = \sum_{i=1}^{N} O(x_i,y_i)S_x(x-x_i)e^{-2jk_c y_i\theta}. \quad (2)$$

In the above expression, $S_x(x-x_i)$ is the down-range point spread function due to the finite-length frequency domain data. Similarly, the cross-range information can also be obtained from angular data via a 1-D Fourier transform of $R(x,\theta)$ along the angular dimension. The resulting image $I(x,y)$ is

$$I(x,y) = \int R(x,\theta)e^{2jk_c y\theta}\,d\theta = \sum_{i=1}^{N} O(x_i,y_i)S_x(x-x_i)\int e^{2jk_c\theta(y-y_i)}\,d\theta = \sum_{i=1}^{N} O(x_i,y_i)S_x(x-x_i)S_y(y-y_i) \quad (3a)$$

where

$$S_y(y-y_i) = \int e^{2jk_c\theta(y-y_i)}\,d\theta \quad (3b)$$

is the cross-range point spread function due to the finite-length angular domain data. If the data are sampled densely enough such that the numerical integration can be carried out accurately, the point-spread function S_y should be a well-localized function with its peak at y_i, while rapidly decaying away from the peak. The resulting image $I(x,y)$ will be a clean image with good indication of the amplitudes and positions of the target point scattering features. However, when the data are undersampled, the numerical integration in (3b) will result in large aliasing error that shows up as high sidelobes in S_y. Consequently, the constructed image will contain strong interference between the scattering features. This effect can be interpreted as the loss of orthogonality of the Fourier bases under the undersampled condition.

In the proposed approach, we use an adaptive feature extraction algorithm in place of the Fourier processing. Instead of projecting the signal onto all the exponential bases simultaneously, we search out the strongest point scattering feature in the cross-range domain and remove it from the original signal. Then the search is repeated for the remainder signal and the point-scattering features are extracted one at a time until the energy of the residue signal is smaller than a preset threshold. The search procedure is carried out by calculating the integral in (3b) for all points in cross range but saving only the maximum value and position, i.e.,

$$[B_p, y_p] = \max_{y_p}\,[I_p(x,y)] \quad (4)$$

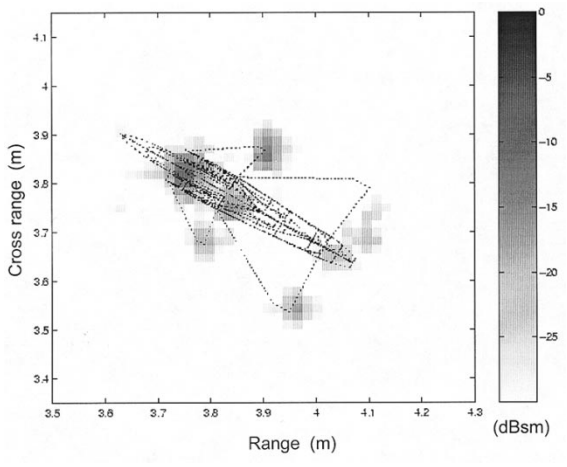

Fig. 1. The ISAR image constructed at 30° azimuth from the original data using FFT.

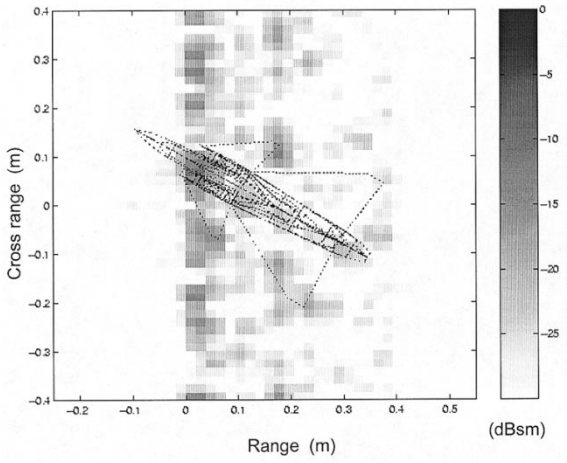

Fig. 2. The ISAR image constructed at 30° azimuth from randomly undersampled data using Fourier transform.

where p denotes the stage of the iterative procedure. The remainder signal is produced by subtracting out the pth feature

$$R_{p+1}(x,\theta) = R_p(x,\theta) - B_p e^{-2jk_c y_p\theta}. \quad (5)$$

The convergence of the above procedure is guaranteed and the mathematical proof is given in [2]. The advantage of such an iterative procedure is that each time we extract out the strongest feature, we also eliminate its interference on the other features. It should be noted that nonuniform sampling is a prerequisite to ensure that there is no ambiguity in the strongest features since uniformly undersampled data will result in multiple positions of the strongest features. For simplicity, the algorithm is repeated for each range cell of the image. A 2-D algorithm in frequency and aspect can also be developed, if the search is carried out for both the range and cross-range parameters. After all the features are extracted out, we can construct an ISAR image using the amplitudes and positions of the point scatterers.

III. Results and Discussion

To examine the applicability of the algorithm on real target scattering data, we reconstruct the radar image of a model (1 : 30 scale) VFY-218 airplane using undersampled chamber measurement data [7]. The measurement data consist of an aspect window from 10° to 50° and a frequency range from 8 to 16 GHz. To construct an ISAR image, we first

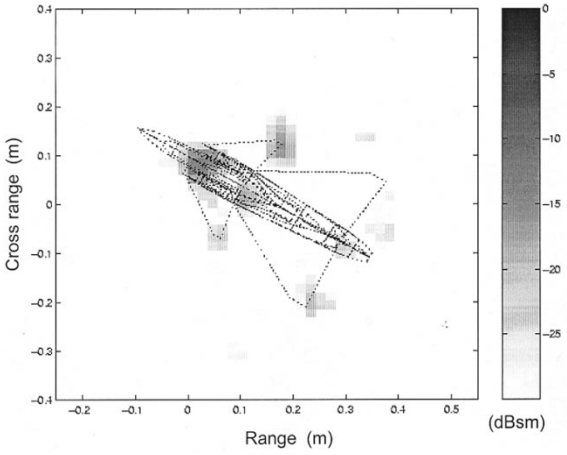

Fig. 3. The ISAR image constructed at 30° azimuth from randomly undersampled data using the AFE algorithm.

polar reformat the frequency-aspect data to the (K_x, K_y) space. The reformatted data consist of 401 samples in K_x and 438 samples in K_y. The ISAR image is first generated by fast Fourier transform (FFT) and shown with the airplane overlay in Fig. 1. The point-scattering features can clearly be seen. Next, we test our algorithm by generating an undersampled data set in K_y. This is approximately the same as undersampling in angle. (Note that for full size targets, this approximation gets better.) The Nyquist sampling rate requires about 36 sampling points in K_y and we randomly select only 24 out of the 438 points. The maximum sampling interval used is about four times the size of the Nyquist sampling interval. Therefore, serious aliasing will occur if the Fourier transform algorithm is used, as shown by the ISAR image displayed in Fig. 2. All the features are overlapped with sidelobe noise such that the point scattering features on the airplane can no longer be distinguished. Next, we apply the adaptive feature extraction (AFE) algorithm to each range cell of the image. The image is reconstructed and shown in Fig. 3. Comparing Fig. 3 with Fig. 1, we can see the main features of the airplane in Fig. 3 are all well reconstructed in Fig. 1. We do observe some noisy spots outside the target at the lower dynamic ranges in Fig. 3. This low-level noise occurs at about 25 dB down from the key features and presents a dynamic range limitation of the present AFE algorithm. The algorithm has also been tested on measured data from in-flight targets with good success.

REFERENCES

[1] D. A. Ausherman, A. Kozma, J. L. Walker, H. M. Jones, and E. C. Poggio, "Developments in radar imaging," *IEEE Trans. Aerosp. Electron. Syst.*, vol. AES-20, pp. 363–400, July 1984.

[2] S. Qian and D. Chen, "Signal regression using adaptive normalized Gaussian functions," *Signal Processing*, vol. 36, pp. 1–11, Mar. 1994.

[3] S. G. Mallat and Z. Zhang, "Matching pursuits with time-frequency dictionaries," *IEEE Trans. Signal Processing*, vol. 41, pp. 3397–3415, Dec. 1993.

[4] L. C. Trintinalia and H. Ling, "Joint time-frequency ISAR using adaptive processing," *IEEE Trans. Antennas Propagat*, vol. 45, pp. 221–227, Feb. 1997.

[5] Y. Wang, H. Ling, and V. C. Chen, "ISAR motion compensation via adaptive joint time-frequency techniques," *IEEE Trans. Aerosp. Electron Syst.*, vol. 34, pp. 670–677, Apr. 1998.

[6] ——, "Application of adaptive joint time-frequency processing to ISAR image enhancement and Doppler feature extraction for targets with rotating parts," in *SPIE Proc. Radar Processing, Technol. Applicat.* San Diego, CA, July 1998, vol. 3462.

[7] "Radar cross section measurement data of the VFY 218 configuration," Naval Air Warfare Center, China Lake, CA, Tech. Rep. NAWCWPNS TM-7621, Jan. 1994.

Electromagnetic Penetration into 2-D Multiple Slotted Rectangular Cavity: TM-Wave

Hyun H. Park and Hyo J. Eom

***Abstract*—Electromagnetic wave penetration into the two-dimensional (2-D) rectangular cavity with multiple slots in an infinite conducting plane with a finite thickness is investigated. The Fourier transform and the mode-matching technique are used to obtain simultaneous equations, which are solved to represent the scattered and the penetrated fields in series forms that are suitable for numerical computations.**

***Index Terms*—Cavity resonator, electromagnetic coupling, slot antenna.**

I. INTRODUCTION

Electromagnetic penetration into the cavity with a slot has been of importance in EMI/EMC-related problems and in the area of target identification [1]–[4]. In this paper, the Fourier transform and the mode-matching technique as used in [5] for electrostatic problem are developed for studying the shielding effectivenesses of the electric and the magnetic fields inside the two-dimensional (2-D) rectangular cavity excited through multiple slots by a TM-polarized plane wave where the electric field vector of the incident wave is parallel to the axis of the shell. The solution presented in this paper is a fast-converging series form, which is numerically efficient. The numerical implementations are taken to illustrate the shielding effectiveness of the slotted rectangular cavity in terms of the size of the cavity and the slot and the number of slots.

II. FIELD REPRESENTATION AND BOUNDARY CONDITIONS

An electromagnetic wave with TM-polarization is obliquely incident on the multiple slotted rectangular cavity as shown in Fig. 1. In region (I), the incident and reflected E-fields are

$$\overline{E}^i(x, y) = -\hat{z} Z_0 e^{ik_x x + ik_y y} \tag{1}$$

$$\overline{E}^r(x, y) = \hat{z} Z_0 e^{ik_x x - ik_y y} \tag{2}$$

where $k_x = k_0 \sin\theta$, $k_y = k_0 \cos\theta$, $k_0 = \omega\sqrt{\mu_0\epsilon_0} = 2\pi/\lambda$ are the free-space wavenumber and Z_0 is the intrinsic impedance in the free-space. The scattered E_z^s-field in region (I) is given by

$$E_z^s(x, y) = \frac{1}{2\pi} \int_{-\infty}^{\infty} \tilde{E}_z^s(\zeta) e^{-i\zeta x + i\kappa y}\, d\zeta \tag{3}$$

where $\kappa = \sqrt{k_0^2 - \zeta^2}$. Assume $\tilde{E}_z^s(\zeta)$ is the Fourier transforms of $E_z^s(x, 0)$ given by $\tilde{E}_z^s(\zeta) = \int_{-\infty}^{\infty} E_z^s(x, 0) e^{i\zeta x}\, dx$.

Manuscript received November 13, 1998; revised November 4, 1999.

H. H. Park is with the Radio Technology Department, Radio and Broadcasting Technology Laboratory, Electronics and Telecommunications Research Institute (ETRI), Kajong Dong, Yusong Gu, Taejon, 305-350 Korea.

H. J. Eom is with the Department of Electrical Engineering, Korea Advanced Institute of Science and Technology (KAIST), Taejon, 305-701 Korea.

Publisher Item Identifier S 0018-926X(00)01658-6.

0018–926X/00$10.00 © 2000 IEEE

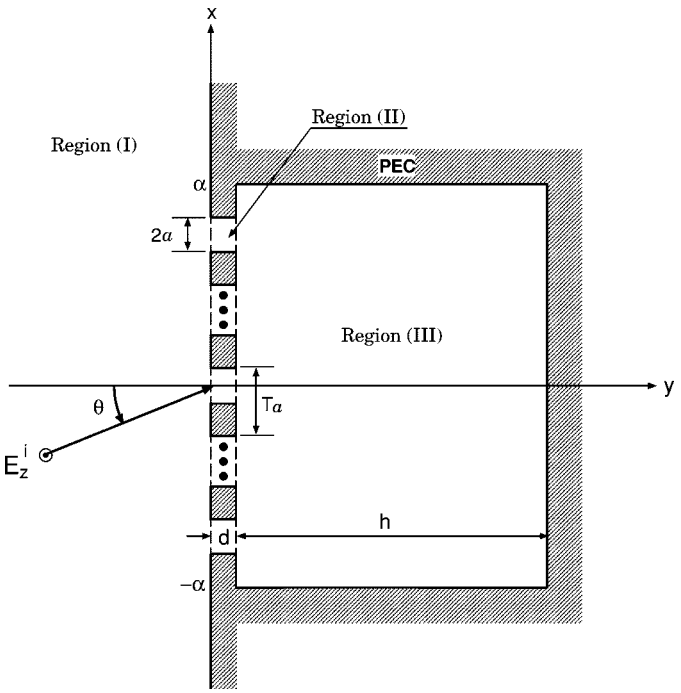

Fig. 1. Geometry of 2-D multiple slotted rectangular cavity: TM-wave.

In region (II) ($|x-lT_a| < a, 0 < y < d$) the electric field $E_z^{\rm II}(x, y)$ inside the slot is

$$E_z^{\rm II}(x, y) = \sum_{m=1}^{\infty} [c_m^l \cos \xi_m(y-d) + d_m^l \sin \xi_m(y-d)] \cdot \sin a_m(x - lT_a + a) \tag{4}$$

where a_m is the $= m\pi/(2a)$ and ξ_m is the $= \sqrt{k_0^2 - a_m^2}$.

In region (III) ($|x| < \alpha, d < y < d+h$) the electric field $E_z^{\rm III}(x, y)$ is

$$E_z^{\rm III}(x, y) = \sum_{n=1}^{\infty} e_n \sin \gamma_n(y-d-h) \sin \alpha_n(x+\alpha) \tag{5}$$

where α_n is the $= n\pi/(2\alpha)$ and γ_n is the $= \sqrt{k_0^2 - \alpha_n^2}$.

To determine the unknown coefficients c_m^l and d_m^l, we enforce the boundary conditions on E_z and H_x at $y = 0$ and d. First, we apply the boundary conditions on E_z and H_x at $y = 0$

$$E_z^i(x, 0) + E_z^r(x, 0) + E_z^s(x, 0) = \begin{cases} E_z^{\rm II}(x, 0), & \text{for } |x - lT_a| < a \\ 0, & \text{elsewhere} \end{cases} \tag{6}$$

and

$$H_x^i(x, 0) + H_x^r(x, 0) + H_x^s(x, 0) = H_x^{\rm II}(x, 0), \quad \text{for } |x - lT_a| < a. \tag{7}$$

Applying the Fourier transform to (6) and solving for $\tilde{E}_z^s(\zeta)$, and then substituting $\tilde{E}_z^s(\zeta)$ into (7), multiplying (7) by $\sin a_p(x - rT_a + a)$ and performing integration from $rT_a - a$ to $rT_a + a$, we obtain the simultaneous equation for c_m^l and d_m^l

$$\frac{a^3 a_p}{2\pi\omega\mu_0} \sum_{l=-L_1}^{L_2} \sum_{m=1}^{\infty} a_m [c_m^l \cos(\xi_m d) - d_m^l \sin(\xi_m d)] I_{mp}^{lr} = \frac{\xi_p}{i\omega\mu_0} [c_p^r \sin(\xi_p d) + d_p^r \cos(\xi_p d)] \delta_{mp} \delta_{lr} - 2a \cos\theta a_p F_p(k_x a) e^{ik_x r T_a}, \qquad p = 1, 2, \cdots \tag{8}$$

where

$$F_m(v) = \frac{(-1)^m e^{iv} - e^{-iv}}{v^2 - (m\pi/2)^2}$$

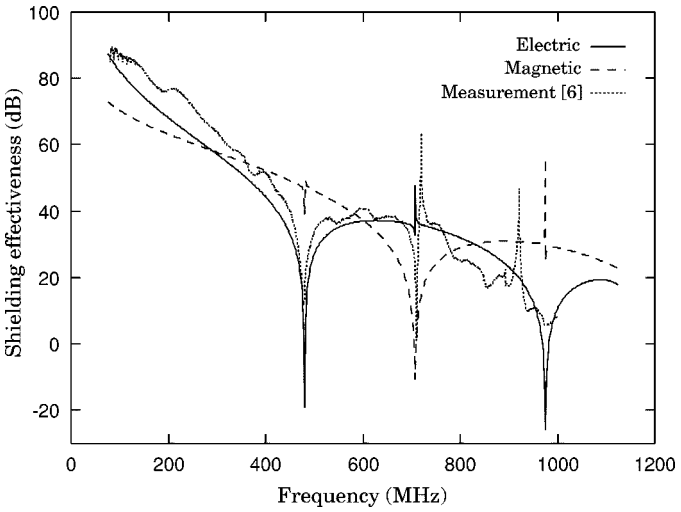

Fig. 2. Shielding effectiveness at the center of a slotted rectangular cavity compared with the measured electric shielding effectiveness of 3-D rectangular cavity (40 × 20 × 50 cm) with an aperture (10 × 2 cm); $a = 5$ cm, $\alpha = 20$ cm, $h = 50$ cm, $d = 0.4$ cm, $\theta = 0°$.

and

$$I_{mp}^{lr} = \int_{-\infty}^{\infty} \kappa F_m(\zeta a) F_p(-\zeta a) e^{i\zeta(l-r)T_a} \, d\zeta. \tag{9}$$

Similarly, by using the boundary conditions at $y = d$, we obtain another simultaneous equation for c_m^l and d_m^l

$$\frac{1}{a\alpha} \sum_{l=-L_1}^{L_2} \sum_{m=1}^{\infty} c_m^l \left\{ \sum_{n=1}^{\infty} \frac{\gamma_n O_{mn}^l O_{pn}^r}{\tan(\gamma_n h)} \right\} = -\xi_p \, d_p^r \tag{10}$$

where

$$O_{mn}^l = \frac{a_m}{\alpha_n^2 - a_m^2} \{\sin[\alpha_n(a - \alpha - lT_a)] + (-1)^m \sin[\alpha_n(a + \alpha + lT_a)]\}. \tag{11}$$

III. Numerical Computations

To illustrate the relation between the field formulation and the resonant modes, $E_z^{\rm III}$ at the center inside the cavity from (5) is roughly given by

$$E_z^{\rm III}(x = 0, y = d + h/2) \sim \sin\left(\frac{n\pi}{2}\right) \sin\left(\gamma_n \frac{h}{2}\right). \tag{12}$$

And the E_z field for the (n, l) mode of the 2-D rectangular cavity without any slot is given by

$$E_z(\text{at the center}) \sim \sin\left(\frac{n\pi}{2}\right) \sin\left(\frac{l\pi}{2}\right). \tag{13}$$

Putting the above equations equal, we can induce the relation as follows:

$$k_0^2 = \alpha_n^2 + \left(\frac{l\pi}{h}\right)^2. \tag{14}$$

Due to the symmetry with respect to the y-axis, only odd numbers are allowed for the index n.

Fig. 2 shows the shielding effectiveness at the center of the 2-D rectangular cavity with a slot, where $a = 5$ cm, $\alpha = 20$ cm, $h = 50$ cm, $d = 0.4$ cm, and $\theta = 0°$. The shielding effectiveness is defined as the ratio of field (electric and magnetic) strengths in the presence and absence of the slotted rectangular cavity.

The resonances at 480.1, 707.7, and 974.7 MHz appear as dips of the electric and the magnetic shielding effectivenesses. The first and the second dips of the electric shielding effectiveness correspond to ($n = 1, l = 1$), and ($n = 1, l = 3$) in (14), respectively, and the dip

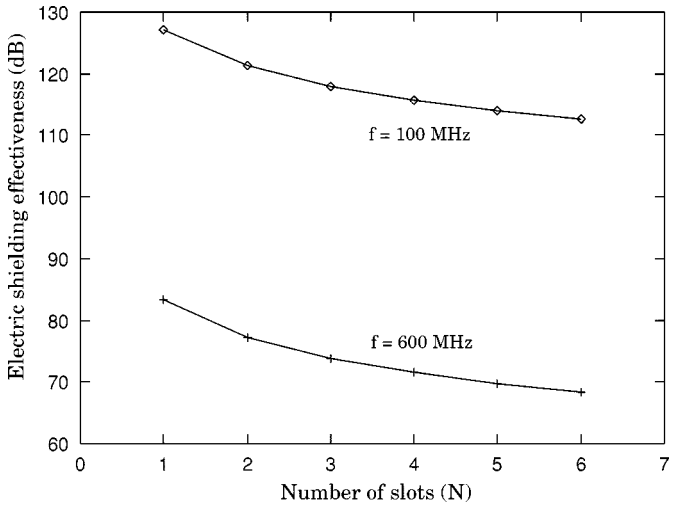

Fig. 3. Electric shielding effectiveness at the center of rectangular cavity with multiple slots as a function of the number of slots; $a = 1$ cm, $T_a = 3a$, $\alpha = 20$ cm, $h = 50$ cm, $d = 0.4$ cm, $\theta = 0^\circ$.

of the magnetic shielding effectiveness corresponds to $(n = 1, l = 2)$ in the same equation.

Fig. 2 also shows that there is good agreement between the electric shielding effectiveness of the 2-D rectangular cavity with a slot and the measured one of the three-dimensional (3-D) rectangular cavity ($40 \times 20 \times 50$ cm) with a aperture (10×2 cm) [6]. The reason of this good agreement is that the dominant electric field vector of the long and thin aperture on the 3-D rectangular cavity is perpendicular to the longer side of the aperture and is approximately uniform along the shorter side. This means that the dominant electric field of the aperture on the 3-D rectangular cavity is effectively equal to the electric field inside the slot of the 2-D rectangular cavity with TM-wave.

Fig. 3 shows the electric shielding effectiveness of the multiple slotted cavity ($a = 1$ cm, $T_a = 3a$, $\alpha = 20$ cm, $h = 50$ cm, $d = 0.4$ cm, and $\theta = 0^\circ$) at 100 and 600 MHz as varying the number of slots. Increasing the total area of slots by adding a slot one by one reduces the shielding effectiveness by about 3 dB each time.

IV. Conclusion

Electromagnetic wave penetration into 2-D multiple slotted rectangular cavity with TM-wave is investigated. By using the Fourier transform and the mode-matching technique, we obtain a solution in a fast-converging series form. Numerical computations are accomplished to show the shielding effectiveness inside the cavity in terms of the size of the cavity and the slot and the number of slots.

References

[1] E. Arvas and T. K. Sarkar, "TM transmission through dielectric-filled slots in a conducting cylindrical shell of arbitrary cross section," *IEEE Trans. Electromagn. Compat.*, vol. EMC-29, pp. 150–156, May 1987.

[2] L. K. Wu and L. T. Han, "E-polarized scattering from a conducting rectangular cylinder with an infinite axial slot filled by a resistively coated dielectric strip," *IEEE Trans. Antennas Propagat.*, vol. 40, pp. 731–733, June 1992.

[3] J. V. Tejedor, L. Nuno, and M. F. Bataller, "Susceptibility analysis of arbitrarily shaped 2-D slotted screen using a hybrid generalized matrix finite-element technique," *IEEE Trans. Electromagn. Compat.*, vol. 40, pp. 47–54, Feb. 1998.

[4] T. M. Wang, A. Cuevas, and H. Ling, "RCS of a partially open rectangular box in the resonant region," *IEEE Trans. Antennas Propagat.*, vol. 38, pp. 1498–1504, Sept. 1990.

[5] H. H. Park and H. J. Eom, "Electrostatic potential distribution through thick multiple rectangular apertures," *Electron. Lett.*, vol. 34, no. 15, pp. 1500–1501, July 1998.

[6] B. W. Kim, Y. C. Chung, and T. W. Kang, "Analysis of electromagnetic penetration through apertures of shielded enclosure using finite element method," in *14th Annu. Rev. Progress Appl. Computat. Electromagn.*, vol. II, Mar. 1998, pp. 795–798.

High-Gain Low-Sidelobe Double-Vee Dipoles

Neal Patwari and Ahmad Safaai-Jazi

***Abstract*—This paper introduces a novel variation of the vee dipole antenna consisting of two coplanar vee dipoles with a common feed point. It is referred to as a *double-vee dipole*. Radiation characteristics of the double-vee dipole antenna are investigated numerically and experimentally. It is shown that the double-vee dipole can provide significantly higher directivity and lower sidelobes and back radiation than the conventional vee dipole. With increasing arm length, the directivity of the double-vee dipole exhibits a series of local maxima. Measured and predicted radiation patterns for a fabricated double-vee dipole are presented and shown to be in good agreement.**

***Index Terms*—Dipole antennas, directive wire antennas, vee antenna.**

I. Introduction

The vee dipole is a well-known geometry developed as a modification to the linear dipole with the aim of increasing its directivity [1]. It has also been shown that by using an arm-shaping technique involving parabolic shapes, the directivity of dipoles can be increased [2]. Double-vee dipole configurations have been investigated for the generation of circularly polarized fields [3]. In such antennas, the vee dipoles have separate feed points and lie in different planes. The double-vee dipole presented here consists of two coplanar vee dipoles with a common feed point. Numerically calculated radiation characteristics and measured far-field radiation patterns are presented in this paper and show that the double-vee dipole can increase directivity and decrease sidelobe level and back radiation compared to the vee dipole. The measurement of the radiation pattern of one double-vee dipole is detailed in this article as a representative case.

II. Design Optimization

A double-vee dipole is specified using four independent geometrical parameters, as shown in Fig. 1. The simulation uses the Numerical Electromagnetics Code v.2 (NEC-2) to perform an exhaustive optimization search. Each possible geometry (with a length granularity of 0.03λ and a angle granularity of 1°) over wide ranges of all four parameters is simulated. The exterior arm length is varied over a range of $1.0\lambda < L_1 < 3.0\lambda$, while the interior arm is kept shorter than exterior arm to limit the footprint: $0 < L_2 < L_1$. The angle of the exterior arm is varied over a range of $3^\circ < \Psi_1 < 90^\circ$, while the interior arm angle Ψ_2 is always at least 3° smaller than Ψ_1. Allowing

Manuscript received October 30, 1998; revised September 15, 1999. This work was supported by a National Science Foundation Graduate Fellowship.

N. Patwari is with Motorola Labs, Plantation, FL 33322 USA.

A. Safaai-Jazi is with the Bradley Department of Electrical and Computer Engineering, Virginia Tech, Blacksburg, VA 24061-0111 USA.

Publisher Item Identifier S 0018-926X(00)01657-4.

0018–926X/00$10.00 © 2000 IEEE

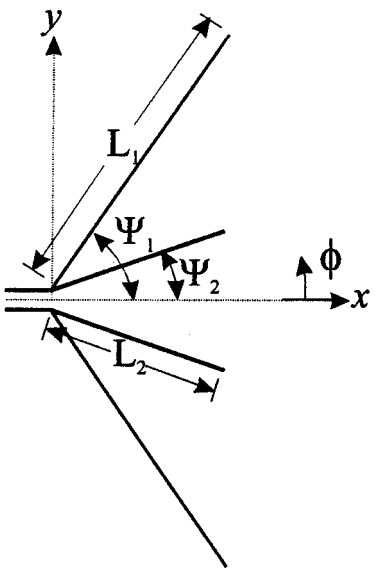

Fig. 1. Geometry and coordinates for the double-vee dipole.

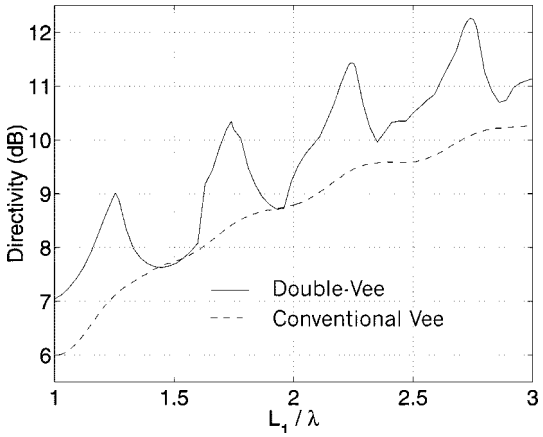

Fig. 2. Variations in maximum directivity versus L_1/λ for conventional and double-vee dipoles.

the arm wires to be closer than 3° to each other would make the antenna difficult to fabricate and also lead to numerical inaccuracies in NEC-2 simulation results.

After tabulating all of the simulation results, geometries are found that produce the highest directivity for each exterior arm length L_1. In Fig. 2, this directivity is plotted. Also plotted, for comparison, is the NEC-2 predicted directivity of a conventional vee dipole with length L_1 and the optimum angle given in [1].

III. Radiation Characteristics

The results in Fig. 2 show that the directivity of the double-vee dipole can be as much as 2.2 dB higher than the conventional vee dipole with the same arm length. It is further observed that as a function of L_1, the directivity of the double-vee dipole exhibits a series of local maxima. The geometries of the double-vee dipoles corresponding to the four local maxima in Fig. 2 are referred to here as the *optimum solutions* and are described in Table I. An antenna designer should use these geometrical parameters to take full advantage of the higher directivity and lower sidelobe and backlobe radiation levels that are possible with the double-vee dipole.

The average front-to-back ratio for the four optimum solutions listed in Table I is 10 dB. For the smallest optimum solutions (#1 and #2), the

TABLE I
Optimum-Directivity Double-Vee Dipole Solutions: Design Parameters and Characteristics

Parameters	Solution 1	Solution 2	Solution 3	Solution 4
L_1	1.255λ	1.745λ	2.245λ	2.740λ
L_2	0.855λ	1.355λ	1.855λ	2.355λ
Ψ_1	53°	44°	38°	35°
Ψ_2	41°	29°	25°	23°
Directivity	8.0	10.8	13.9	16.8
3dB Beamwidth	24°	20°	18°	16°
Max Sidelobe Level	-8.6 dB	-9.0 dB	-10.3 dB	-9.3 dB
Front/Back Ratio	11.9 dB	10.1 dB	10.3 dB	9.3 dB
3dB Bandwidth	11.0%	7.2%	5.8%	4.7%
Input Resistance	341Ω	388Ω	386Ω	395Ω
Input Reactance	163Ω	110Ω	106Ω	98Ω

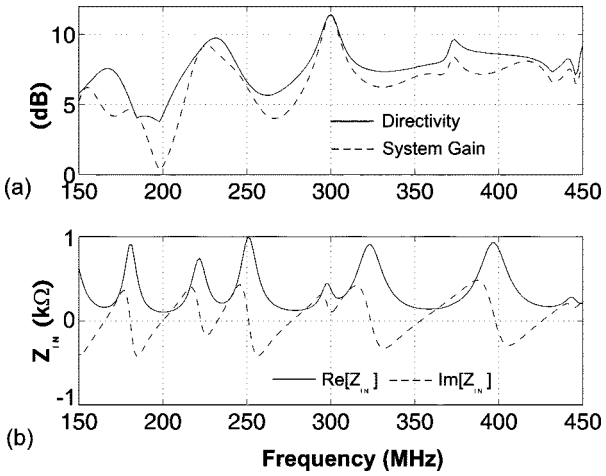

Fig. 3. (a) Directivity, antenna system gain (directivity minus reflection loss). (b) Input impedance versus frequency for optimum solution #3 designed for $f_c = 300$ MHz.

backlobe is lower than the other sidelobes. With each larger optimum solution, the backlobe radiation level increases while the other sidelobe levels decrease. Overall, the beamwidth decreases and the directivity increases, even as the front-to-back ratio decreases. The backlobe radiation level of the double-vee dipole is about 7 dB lower than that of a conventional vee dipole [1]. It is particularly interesting that the optimum solutions have L_1 and L_2 that increment by approximately $\lambda/2$ for each larger solution. It can be inferred from these results that even larger, more directive optimum solutions can be found by successively raising L_1 and L_2 by $\lambda/2$ and then finding the optimum Ψ_1 and Ψ_2. The input impedance has a significant reactive component that arises from the resonant nature of the double-vee dipole. The real and imaginary parts of the input impedance are about 400 and 100Ω, respectively, at the center frequencies of optimum solutions two, three, and four. Fig. 3(b) shows the input impedance of a double-vee dipole designed for optimum solution #3 at a center frequency $f_c = 300$ MHz. To show the effects of the input impedance on the bandwidth, the an-

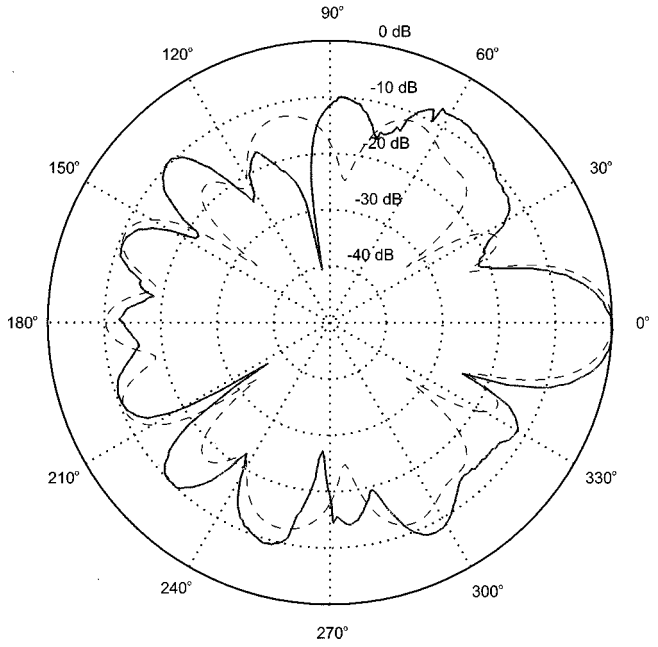

Fig. 4. Predicted (– – – –) and measured (——) E-plane radiation pattern, optimum solution #3 with parameters given in Table I with $\lambda = 12.5$ cm.

tenna is matched to a 300Ω transmission line by means of a short-circuit single-stub tuner. The tuner is arranged such that the double-vee dipole is perfectly matched to 300Ω at the antenna's center frequency. Fig. 3(a) plots the directivity of the antenna and the antenna system gain (the directivity minus the reflection loss) versus frequency. The 3-dB bandwidth of each optimum solution double-vee dipole, assuming that a short-circuit single-stub tuner is used for perfect matching at f_c is given in Table I. Note from Fig. 3(a) that a double-vee dipole designed for maximum directivity at 300 MHz can also be operated at other frequencies. Different multiband characteristics are possible with each optimum solution.

Measurements of all four optimum solution double-vee dipoles were conducted. Each was constructed using aluminum wire with a diameter of 3 mm and mounted on thin cardboard. The double-vee dipole at the optimum solution #1 was constructed with $\lambda = 20$ cm and measured at 1.5 GHz and was presented in the preliminary phase of our research [4]. The other three double-vee dipoles were built with $\lambda = 12.5$ cm and measured at 2.4 GHz. Fig. 4 shows the measured far-field E-plane pattern in decibels for optimum solution #3. The measured and predicted half-power beamwidths are the same at 18°. The measured back radiation level is more than 10 dB below the main lobe peak. Also shown in Fig. 4 are the numerically calculated radiation patterns from NEC-2. The measured and predicted patterns for all four optimum solutions show similar agreement.

IV. Conclusions

The double-vee dipole is as compact and low-cost as the vee dipole but has significant advantages. In this paper, a series of optimum solutions for the double-vee dipole are presented that yield sidelobe and backlobe radiation level reductions of up to 7 dB and directivity increases of 2.2 dB compared to the vee dipole. The double-vee dipole is also shown to be well suited for multiband operation. Radiation properties of the optimum solutions are investigated both numerically and experimentally. Since measured results accurately match numerical results, the double-vee dipole promises simple and predictable design and construction. The calculated and measured results both suggest that the double-vee dipole is a promising candidate for applications, where the bandwidth requirement is modest and higher gain and lower sidelobe and backlobe levels are desired to reduce interference effects and, hence, improve the quality of information signals.

Acknowledgment

The authors would like to thank M. Barts and R. Neely of the Virginia Tech Antenna Laboratory for the measurements.

References

[1] G. A. Thiele and E. P. Ekelman, "Design formulas for vee dipoles," *IEEE Trans. Antennas Propagat.*, vol. AP-28, pp. 588–590, July 1980.
[2] D. K. Cheng and C. H. Liang, "Shaped wire antennas with maximum directivity," *Electron. Lett.*, vol. 18, Sept. 16, 1982.
[3] H.-W. Tseng and B. A. Munk, "The generation of omnidirectional circularly polarized far field by a pair of orthogonally oriented vee dipoles," in *AP-S Int. Symp.*, vol. 2, Ann Arbor, MI, July 1993, pp. 1042–1045.
[4] H. Patwari and A. Safaai-Jazi, "Predictions and measurements of double-vee dipoles," in *AP-S Int. Symp.*, vol. 3, Atlanta, GA, June 1998, pp. 1426–1429.
[5] W. L. Stutzman and G. A. Theile, *Antenna Theory and Design*, 2nd ed. New York: Wiley, 1998.

Exact Geometrical Optics Solution for an Isorefractive Wedge Structure

Piergiorgio L. E. Uslenghi

***Abstract*—A structure consisting of four right-angle wedges with a common edge, made of four different materials isorefractive to one another is considered. If a certain relation is satisfied among the four intrinsic impedances of the materials, then an incident plane wave generates reflected and transmitted plane waves that constitute the exact solution to the boundary-value problem. This geometrical-optics exact solution is valid for arbitrary polarization and arbitrary direction of incidence of the primary wave.**

***Index Terms*—Complex media, electromagnetic diffraction, electromagnetic reflection and transmission, geometrical optics, isorefractive material.**

I. Introduction

Boundary-value problems involving isorefractive materials and for which geometrical optics represents the exact solution have been solved for a wedge structure [1] and a paraboloid [2] under plane wave excitation and for an isolated wedge with a line source at its edge [3]. In this letter, a new solution is presented for a structure consisting of four 90° wedges with a common edge, each filled with a linear, homogeneous, and isotropic material. The four materials are isorefractive to one another. It is shown that geometrical optics yealds the exact solution when the primary source is a plane wave with arbitrary direction of incidence and arbitrary polarization, provided that a certain relation is satisfied among the intrinsic impedances of the four materials. This new solution was presented recently at a symposium [4].

Manuscript received October 20, 1998; revised October 26, 1999.

The author is with the Department of Electrical Engineering and Computer Science, University of Illinois at Chicago, Chicago, IL 60607-7053 USA.

Publisher Item Identifier S 0018-926X(00)01659-8.

0018–926X/00$10.00©2000 IEEE

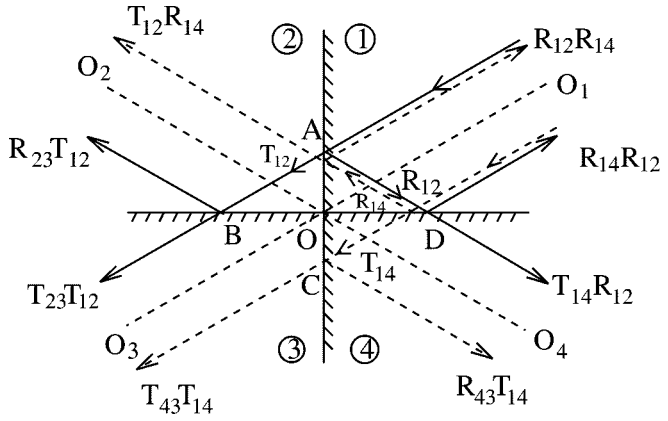

Fig. 1. Geometry of the problem.

Consider the geometry shown in Fig. 1. The space is divided into four quadrants by the two planes AOC and BOD perpendicular to each other. Fig. 1 is a cross section of the structure, perpendicular to the common edge O of the four 90° wedge regions. Each quadrant is filled with a linear, homogeneous, and isotropic material of electric permittivity ε and magnetic permeability μ such that

$$\varepsilon_h \mu_h = \varepsilon_l \mu_l, \qquad (h, l = 1, 2, 3, 4) \tag{1}$$

i.e., the four wedge regions are isorefractive to one another, but have different intrinsic impedances given by

$$Z_l = \sqrt{\frac{\mu_l}{\varepsilon_l}}, \qquad (l = 1, 2, 3, 4). \tag{2}$$

For incidence from quadrant h of intrinsic impedance Z_h on the interface separating it from quadrant l of intrinsic impedance Z_l, the reflection coefficient R_{hl} and the transmission coefficient T_{hl} are given by

$$R_{hl} = \frac{Z_l - Z_h}{Z_l + Z_h}, \quad T_{hl} = \frac{2Z_l}{Z_l + Z_h} \tag{3}$$

and are independent of both direction of incidence and polarization of the incident wave.

A plane wave with electric field of unit amplitude and propagating inside the first quadrant in the direction O_1O perpendicular to the edge is reflected and transmitted at the interfaces OA between the first and second quadrants and OD between the first and fourth quadrants. Incidence on OA generates a reflected plane wave propagating from A to D with amplitude R_{12} and a plane wave transmitted into the second quadrant and propagating from A to B with amplitude T_{12}. The reflected wave incident on the interface OD with amplitude R_{12} is partly reflected into the first quadrant with amplitude $R_{14}R_{12}$ and partly transmitted into the fourth quadrant with amplitude $T_{14}R_{12}$. The transmitted wave incident on the interface OB with amplitude T_{12} is partly reflected into the second quadrant with amplitude $R_{23}T_{12}$ and partly transmitted into the third quadrant with amplitude $T_{23}T_{12}$. Similar considerations apply to that portion of the primary plane wave that is incident from the first quadrant on the interface OD between the first and fourth quadrants. All incident, reflected, and transmitted waves are shown with their amplitudes in the ray tracing of Fig. 1.

The total field in the first quadrant consists of four plane waves: the incident wave propagating in the direction O_1O with unit amplitude, a doubly reflected wave propagating in the direction OO_1 with amplitude $R_{12}R_{14}$, a reflected wave propagating in the direction AD with amplitude R_{12}, and a reflected wave propagating in the direction DA with amplitude R_{14}.

The total field in the second quadrant is the superposition of two fields: a transmitted plane wave propagating in the direction AB with amplitude T_{12} and a field propagating in the direction OO_2 that constitutes a plane wave only if no discontinuity occurs across the semiplane OO_2; that is, if

$$R_{23} = R_{14}. \tag{4}$$

Similarly, the total field in the fourth quadrant is the sum of a transmitted plane wave propagating in the direction DC with amplitude T_{14} and of a field propagating in the direction OO_4; that is, a plane wave if

$$R_{12} = R_{43}. \tag{5}$$

Finally, the field in the third quadrant is a plane wave propagating in the direction of incidence OO_3 if

$$T_{23}T_{12} = T_{43}T_{14}. \tag{6}$$

With the use of (3), it is easily proven that conditions (4)–(6) are satisfied if and only if

$$Z_1 Z_3 = Z_2 Z_4. \tag{7}$$

If this condition is not satisfied, then diffraction occurs at the common edge of the four wedges and geometrical optics no longer represents the exact solution. Relation (7) may be rewritten with the aid of (1) and (2) as

$$\varepsilon_1 \varepsilon_3 = \varepsilon_2 \varepsilon_4 \tag{8}$$

or, equivalently, as

$$\mu_1 \mu_3 = \mu_2 \mu_4. \tag{9}$$

If condition (7) [or (8), or (9)] is satisfied, then the total field in each quadrant is the sum of plane waves, the boundary conditions are satisfied, the edge does not scatter and geometrical optics is the exact solution of the boundary-value problem. Although this solution was derived for incidence normal to the edge, it is easily extended to oblique incidence by applying the result obtained in [5]. This is the only presently known case in which the exact scattering by a penetrable-wedge structure is given by the geometrical optics solution for any direction of incidence and any polarization of the primary plane wave.

REFERENCES

[1] P. L. E. Uslenghi, "Exact solution for a penetrable wedge structure," *IEEE Trans. Antennas Propagat.*, vol. 45, p. 179, Jan. 1997.

[2] S. Roy and P. L. E. Uslenghi, "Exact scattering for axial incidence on an isorefractive paraboloid," *IEEE Trans. Antennas Propagat.*, vol. 45, p. 1563, Oct. 1997.

[3] V. G. Daniele and P. L. E. Uslenghi, "Closed-form solution for a line source at the edge of an isorefractive wedge," *IEEE Trans. Antennas Propagat.*, vol. 47, pp. 764–765, Apr. 1999.

[4] P. L. E. Uslenghi, "Exact geometrical optics scattering by an isorefractive wedge structure," in *Dig. IEEE Antennas Propagat. Soc. Int. Symp.*, Atlanta, GA, June 1998, p. 870.

[5] ——, "TE-TM decoupling for scattering from isorefractive cylinders of arbitrary shape," in *Proc. Int. Symp. Electromagn. Theory*, Thessaloniki, Greece, May 1998, pp. 432–433.

Near-Field Signature Prediction Using Far-Field Scattering Centers Extracted from the Shooting and Bouncing Ray Technique

Rajan Bhalla and Hao Ling

***Abstract*—We present a technique to predict the near-field radar cross section (RCS) of a target using the far-field scattering centers extracted from the shooting and bouncing ray (SBR) technique. The results generated using this methodology are verified against the brute-force SBR calculations for near-field scenarios. It is demonstrated that this technique is a fairly accurate and very efficient way to generate near-field RCS data provided that the transceiver is not very close to the target.**

***Index Terms*—Radar, ray shooting, scattering centers, target identiification.**

I. Introduction

For many radar applications the transmitting and receiving antennas are located in the near-field zone of the target. Under this situation, the distance between the transmitting antenna and the target may not be large enough to treat the incident field arriving at the target as a plane wave. Similarly, the distance between the receiving antenna and the target may not be large enough to treat the scattered field arriving at the receiver as a plane wave. Hence, the far-field assumption is not valid and a near-field analysis is necessary. One of the existing methodologies to compute near-field radar cross section (RCS) is to use the shooting and bouncing ray (SBR) technique [1], [2]. In the SBR technique, rays are launched at the target from the phase center of the transmitting antenna and are traced according to the law of geometrical optics. At the exit point of each ray, a ray-tube integration is performed to find its contribution to the total scattered field at the receiving antenna, taking into account of the distance from the ray tube to the receiver location. Although the SBR methodology is straightforward, for typical radar applications the problem involved often contains a large number of parameter combinations. For example, in typical missile engagement simulations, the scattered field is of interest at different transceiver locations and for different antenna patterns. Each combination is a new problem and requires that the whole computation be carried out each time. This can lead to an inordinately large amount of computation time. In this letter, we present a technique to predict the near-field RCS of a target by taking advantage of the far-field scattering centers extracted using the existing capability of the SBR technique [3], [4]. The basic idea is to extract the far-field three-dimensional (3-D) scattering centers once and then use the strengths and positions of the extracted scattering centers to reconstruct the near-field RCS at different transceiver locations. Since the extraction is done only at the far-field range and the reconstruction can be carried out very quickly, this methodology is potentially a very efficient way to compute near-field RCS.

II. Near-Field RCS Prediction Using Far-Field Scattering Centers

It is well known that the scattered far field from an electrically large target can be modeled by a discrete set of scattering centers on the target [see Fig. 1(a)]. The monostatic 3-D scattering centers at a given incident direction can be sparsely represented by a set of numbers $\{A_n, \boldsymbol{R}_n\}$, where A_n is the strength of a scattering center and $\boldsymbol{R}_n$ is its 3-D location. The 3-D scattering center extraction methodology of a target using the SBR technique has been developed recently in [3] and [4]. To predict near-field data using the far-field scattering centers, we argue that each scattering center models the interaction between the incident electromagnetic wave and a localized portion of the target. The portion of the target that gives rise to each scattering center is much smaller than the whole target. Consequently, the scattering phenomenon represented by each scattering center is expected to be valid at a distance much closer than the usual far-field range criterion of $L = 2D^2/\lambda$, where D is the maximum target dimension and λ is the wavelength. At very closed-in ranges the scattering centers themselves will be defocused and this interpretation may no longer be valid.

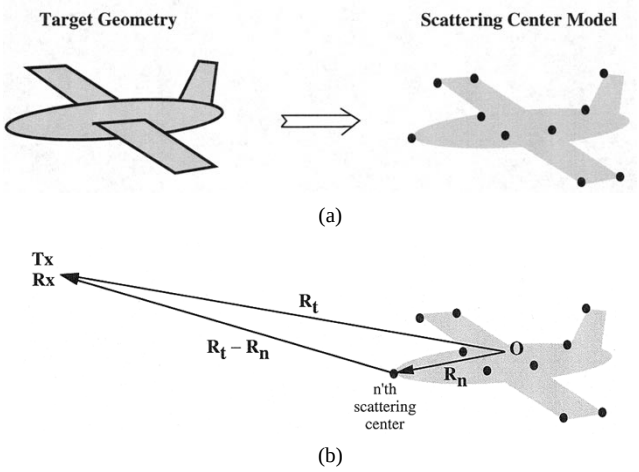

Fig. 1. (a) Three-dimensional far-field scattering center model of a target. (b) Near-field RCS prediction based on far-field scattering centers.

Next, we provide the formula to reconstruct the monostatic near-field from the monostatic far-field scattering centers. To reconstruct the scattered field, E^s at a frequency f for a transceiver located at R_t, we sum up the contribution of each scattering center as [see Fig. 1(b)]

$$E^s(f, \boldsymbol{R}_t) = \sum_n A_n \exp\left(-j\frac{4\pi f}{c}|\boldsymbol{R}_t - \boldsymbol{R}_n|\right) \cdot \left\{\frac{\boldsymbol{R}_t^2}{|\boldsymbol{R}_t - \boldsymbol{R}_n|^2}\right\}. \quad (1)$$

Notice that in addition to the phase term to take into account of the near-field effect, we also use a range correction for the amplitude of each scattering center. The scattered field defined in (1) has been normalized so that it will reduce to the far-field RCS as $\boldsymbol{R}_t$ approaches the far-field range [5], [6]. If the antenna pattern is not isotropic, the effect of the antenna pattern can also be accounted for in (1). In addition, although only the monostatic scattering is considered in this paper, the methodology is extendible to the more general bistatic scenario. It should also be noted that the reconstruction in (1) is based on single-bounce scattering mechanisms and is not very accurate for scattering centers whose contribution comes from high multibounce mechanism.

III. Results

Two numerical examples are presented to demonstrate the accuracy of this technique. The reconstructed near-field RCS from far-field scattering centers is compared to the brute-force SBR results as a function

Manuscript received December 31, 1997.

R. Bhalla was with the University of Texas at Austin, Austin, TX 78712-1084 USA. He is now with SAIC-DEMACO, Boston, MA 01880 USA.

H. Ling is with the Department of Electrical and Computer Engineering, the University of Texas at Austin, Austin, TX 78712-1084 USA.

Publisher Item Identifier S 0018-926X(00)01282-5.

0018–926X/00$10.00 © 2000 IEEE

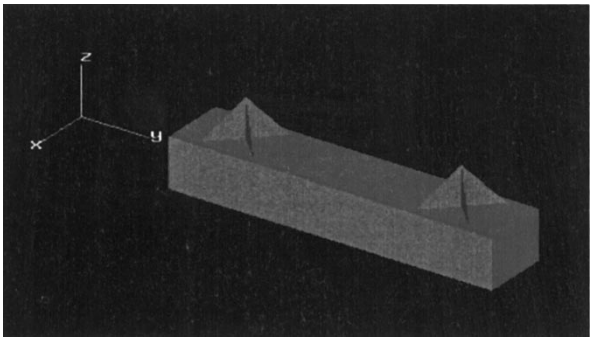

(a)

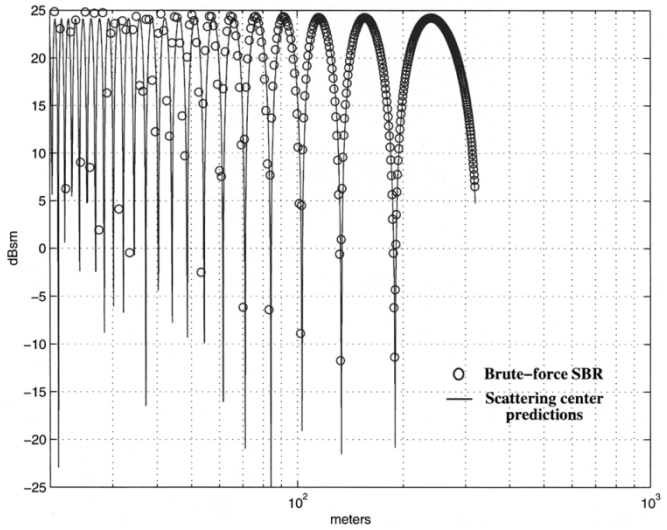

(b)

Fig. 2. Comparison of the near-field RCS computed by brute-force SBR and by scattering center prediction for a conical target. (a) Target geometry. (b) Near-field RCS versus range.

of range of the transceiver. The antenna pattern of the transceiver is assumed to be isotropic and horizontally polarized. The first example is a simple canonical target comprising of two triplates mounted on an elongated box as shown in Fig. 2(a). The monostatic 3-D scattering centers are extracted at an incident azimuth angle of -15° and an elevation angle of 15°. The far-field criterion for this 3-m target is 760 m at 12.65 GHz. The near-field RCS is computed as the transceiver is moved closer to the target at the same fixed incident angle of (-15°, 15°) and the range was varied from 320 to 15 m. Fig. 2(b) shows the near-field RCS comparison between the brute-force computation and the scattering center reconstruction plotted on a logarithmic scale of the range. The agreement between the two profiles is very good, even up to a very closed-in range of 50 m. The pattern observed in the RCS profile is consistent with the beating of two strong scattering centers at the two triplate positions.

The second example is a full-size airplane. The monostatic 3-D scattering centers are extracted at an incident (AZ, EL) angle of (120°, -18°). The far-field distance for this 20-m target is 27 000 m at 10 GHz. The near-field RCS is computed as the transceiver is moved closer to the target at the same fixed incident angle of (120°, -18°) and the range was varied from 25 000 to 200 m. Fig. 3 shows the near-field RCS comparison between the brute-force SBR computation and the scattering center reconstruction plotted on a logarithmic scale of range. Even though this target has some multibounce returns from inlet ducts whose reconstruction will not be very accurate using scattering center predictions, the reconstructed RCS captures the salient feature of the brute-force SBR computation. The comparison degrades as we get closer to the target. In terms of computation time, the brute-force computation takes roughly 30 min/range point on an SGI R4400 workstation. The scattering center extraction itself can be carried out in about 30 min. Once the scattering centers are extracted, however, the reconstruction can be done in seconds at all the range values. Hence, the scattering centers offer tremendous computation time savings for the computation of near-field RCS.

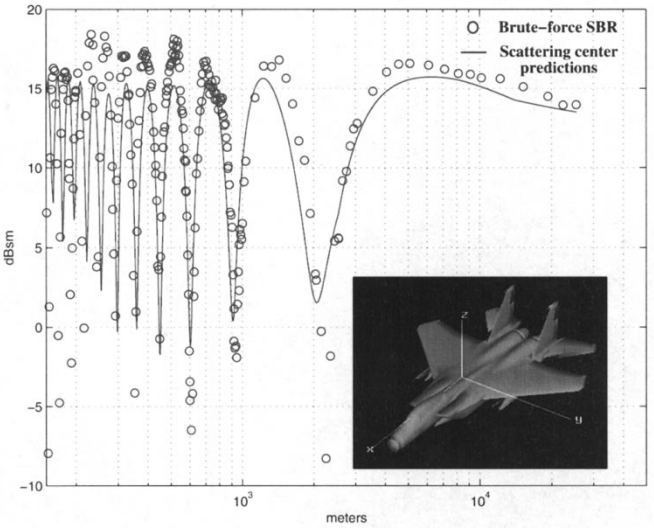

Fig. 3. Comparison of the near-field RCS computed by brute-force SBR and by scattering center prediction for a full-size airplane.

IV. Conclusion

In this paper, we presented an efficient technique to predict near-field RCS using far-field scattering centers extracted from the SBR technique. Such a scheme allows us to generate the near-field RCS in real time for a variety of input parameters such as range and antenna patterns. For very closed-in ranges, however, this scheme is expected to break down as the scattering centers become defocused. In addition, such prediction is based on single-bounce scattering and will not be as accurate for multibounce returns. Although only near-field monostatic scattering is considered in this paper, the methodology can be extended to handle more general bistatic scenarios.

References

[1] C. L. Yu, R. Kipp, D. J. Andersh, and S. W. Lee, "Near-field electromagnetic modeling and analysis," in *IEEE Antennas Propagat. Symp. Dig.*, Montreal, Canada, July 1997, pp. 1168–1171.

[2] S. K. Jeng, "Near-field scattering by physical theory of diffraction and shooting and bouncing rays," in *1997 IEEE Antennas Propagat. Symp. Dig.*, Montreal, Canada, July 1997, pp. 1176–1179.

[3] R. Bhalla and H. Ling, "3-D scattering center extraction using the shooting and bouncing ray technique," *IEEE Trans. Antennas Propagat.*, vol. 44, pp. 1445–1453, Nov. 1996.

[4] R. Bhalla, J. Moore, and H. Ling, "A global scattering center representation of complex targets using the shooting and bouncing ray technique," *IEEE Trans. Antennas Propagat.*, vol. 45, pp. 1850–1856, Dec. 1997.

[5] S. W. Lee and S. K. Jeng, *NcPTD 1.2—A High Frequency Near-Field RCS Computation Code Based on Physical Theory of Diffraction*. Champaign, IL: DEMACO Inc., June 1991, vol. 6.

[6] J. M. Taylor and A. J. Terzuoli, "On the concept of near-field radar cross section," in *1997 IEEE Antennas Propagat. Symp. Dig.*, Montreal, Canada, July 1997, pp. 1172–1175.

Matrix-Exponent Formulations for Wave Radiation and Propagation in Anisotropic Stratified Ionosphere

M. Y. Xia and Z. Y. Chen

***Abstract*—A matrix-exponent method is developed to treat wave radiation and propagation in anisotropic stratified ionosphere. By using matrix-exponent formulations, the present approach is relatively compact for expressions and reliable for computations. As an example, the method is used to calculate the ELF excitation of the earth-ionosphere waveguide by an equivalent dipole resulted from heating the lower ionosphere with modulated HF waves. Simulation results are presented and compared for different latitudes.**

***Index Terms*—Anisotropic media, electromagnetic propagation, ELF propagation, ionosphere.**

I. Introduction

One aspect to study the wave radiaton and propagation in ionosphere in recent years is to calculate the ELF radiations produced by heating the lower ionosphere with powerful modulated HF waves, which, to some extent, has been demonstrated to be feasible [1], [2]. In order to obtain some explicit forms, a few simplified models such as neglecting the geomagnetic effects [3] were adopted. A more practical anisotropic multilayered model was used by Yagitani *et al.* [4], but their numerical techniques previously developed by Nagano *et al.* [5] were actually hard to master. There is a general dyadic method proposed by Habashy *et al.* [6]; this method is unfortunately too complicated to code for computations.

In this letter, a new approach using matrix-exponent formulations is deveolped, which is comparatively elegant for expressions and reliable for computations. By directly dealing with matrix exponent, which is an intrinsic function in some languages such as Mathematica, many matrix-handling difficulties are actually avoidable. To overcome the troublesome numerical swamping problem, a useful scale-down trick is introduced, which is helpful for us to extract stable solutions. As an example, the present approach is used to calculate the ELF excitation of the earth-ionosphere waveguide by an dipole source in the lower ionosphere. Simulation results are presented and compared for three areas, Tromsø (Norway), Beijing and Haikou (China), with latitudes 79°, 40°, and 20°, respectively.

II. The Approach

Refer to Fig. 1. Suppose that the radiation source is a dipole $\boldsymbol{P}$ located at z_s above the ground and the time dependence is $e^{-j\omega t}$. The Maxwell equations for the present problem are

$$\begin{cases} \nabla \times \boldsymbol{E} = j\omega\mu_0 \boldsymbol{H} \\ \nabla \times \boldsymbol{H} = \boldsymbol{J}_s - j\omega\epsilon_0 \overline{\boldsymbol{K}} \cdot \boldsymbol{E} \end{cases} \tag{1}$$

where $\boldsymbol{J}_s = \boldsymbol{P}\delta(x)\delta(y)\delta(z - z_s)$ and $\overline{\boldsymbol{K}}$ is a [3 × 3] matrix—the relative dielectric tensor of the medium.

Taking Fourier transform of (1) in horizontal directions with respect to $(x, y) \leftrightarrow (k_0 S_x, k_0 S_y)$ and eliminating E_z and H_z we have

$$\frac{d\boldsymbol{V}}{dz} = jk_0 \overline{\boldsymbol{Q}} \cdot \boldsymbol{V} + \boldsymbol{V}_s \delta(z - z_s) \tag{2}$$

Manuscript received April 17, 1997. This work was supported by the National Natural Science Foundation of China.

The authors are with the Institute of Electronics, Academia Sinica, Beijing, 100080 China.

Publisher Item Identifier S 0018-926X(00)02624-7.

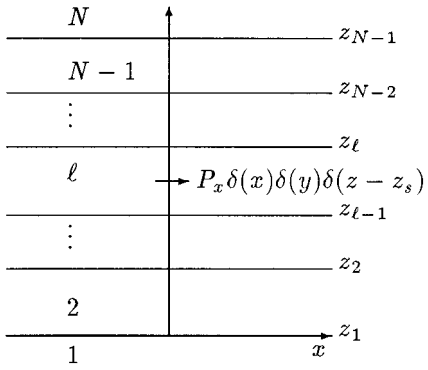

Fig. 1. Configuration of the stratified ionosphere. The first layer is the earth and the Nth layer is outer space, while the source is lacated in the ℓth layer. X eastward, Y northward, and Z upward.

where $k_0 = \omega\sqrt{\epsilon_0\mu_0}$ is the wave number in free-space, $\boldsymbol{V} = [E_x, -E_y, Z_0 H_x, Z_0 H_y]^T$ is a column vector representing the tangential components of the fields, $\boldsymbol{V}_s = Z_0[0, 0, 0, -P_x]^T$ reflects the source, $Z_0 = 120\pi$ is the wave impedance in free-space, and (3), shown at the bottom of the next page, with $K_{ij}(i, j = 1, 2, 3)$ the elements of the dielectric tensor $\overline{\boldsymbol{K}}$.

The solution to (2) can be expressed in matrix-exponent form as

$$\boldsymbol{V}(z) = \begin{cases} [\boldsymbol{a}_1 \ \ \boldsymbol{a}_2] \cdot \boldsymbol{C}_1, & z = z_1 = 0 \\ \exp[jk_0 \overline{\boldsymbol{Q}}_i (z - z_s)] \cdot \boldsymbol{C}_i, & \\ \quad z_{i-1} \le z \le z_i, \ i \ne 1, \ell, N & \\ \exp[jk_0 \overline{\boldsymbol{Q}}_\ell (z - z_s)] \cdot \left(\boldsymbol{C}_\ell \pm \frac{1}{2}\boldsymbol{V}_s\right), & \\ \quad z_s < z \le z_\ell, \ z_{\ell-1} \le z < z_s & \\ [\boldsymbol{a}_3 \ \ \boldsymbol{a}_4] \cdot \boldsymbol{C}_N, & z = z_{N-1} \end{cases} \tag{4}$$

where $\boldsymbol{a}_1$ and $\boldsymbol{a}_2$ are two appropriate eigenvectors of $\overline{\boldsymbol{Q}}_1$, so are $\boldsymbol{a}_3$ and $\boldsymbol{a}_4$ of $\overline{\boldsymbol{Q}}_N$. $\boldsymbol{C}_1$ and $\boldsymbol{C}_N$, which are [2 × 1] vectors, and $\boldsymbol{C}_i (i = 2, 3, \cdots, N - 1)$, which are [4 × 1] vectors, are constant vectors to be determined by boundary conditions. To express the solution in matrix-exponent form, which is an intrinsic function in some languages such as Mathematica can avoid many numerical troubles that must arise if solving the eigen-problem of matrix $\overline{\boldsymbol{Q}}$ in each layer.

Let $\overline{\boldsymbol{P}}_i(z - z') = \exp[jk_0 \overline{\boldsymbol{Q}}_i (z - z')](z_{i-1} \le z, z' \le z_i)$. Because the vector $\boldsymbol{V}$ must be continuous at the interfaces, from (4) we have

$$\begin{cases} \boldsymbol{V}(z_s^-) = \left(\boldsymbol{C}_\ell - \frac{1}{2}\boldsymbol{V}_s\right) = \overline{\boldsymbol{D}} \cdot \boldsymbol{C}_1 \\ \boldsymbol{V}(z_s^+) = \left(\boldsymbol{C}_\ell + \frac{1}{2}\boldsymbol{V}_s\right) = \overline{\boldsymbol{U}} \cdot \boldsymbol{C}_N \end{cases} \tag{5}$$

where (6), shown at the bottom of the next page. So $\overline{\boldsymbol{D}}$ and $\overline{\boldsymbol{U}}$ are [4 × 2] matrices. From (5), we get

$$\begin{cases} \overline{\boldsymbol{U}} \cdot \boldsymbol{C}_N - \overline{\boldsymbol{D}} \cdot \boldsymbol{C}_1 = \boldsymbol{V}_s \\ \overline{\boldsymbol{U}} \cdot \boldsymbol{C}_N + \overline{\boldsymbol{D}} \cdot \boldsymbol{C}_1 = 2\boldsymbol{C}_\ell \end{cases} \tag{7}$$

hence

$$\boldsymbol{C}_\ell = \tfrac{1}{2}[\overline{\boldsymbol{U}} \ \ \overline{\boldsymbol{D}}] \cdot [\overline{\boldsymbol{U}} \ \ -\overline{\boldsymbol{D}}]^{-1} \cdot \boldsymbol{V}_s. \tag{8}$$

It should be noted that we calculate $\boldsymbol{C}_\ell$ instead of $\boldsymbol{C}_1$ and $\boldsymbol{C}_N$, which are highly unstable. The matrices $\overline{\boldsymbol{D}}$ and $\overline{\boldsymbol{U}}$ are always good-posed and can be scaled down at any moment when they are being calculated backwardly from (6); that is, $\overline{\boldsymbol{D}}$ and $\overline{\boldsymbol{U}}$ can be replaced by $\overline{\boldsymbol{D}} \cdot \overline{\mathbf{A}}$ and $\overline{\boldsymbol{U}} \cdot \overline{\mathbf{B}}$, respectively, where $\overline{\boldsymbol{A}}$ and $\overline{\boldsymbol{B}}$ are arbitrary [2 × 2] nonsingular

0018–926X/00$10.00 © 2000 IEEE

matrices, the result of $\boldsymbol{C}_\ell$ will remains unchange. This scale-down trick is useful to avoid numerical swamping.

The vector $\boldsymbol{V}$ at z assumed in the kth layer given $\boldsymbol{C}_\ell$ by (8) is

$$\boldsymbol{V}(z) = \begin{cases} \overline{\boldsymbol{P}}_D(z,\, z_s) \cdot \left(\boldsymbol{C}_\ell - \frac{1}{2}\boldsymbol{V}_s\right), & z < z_s \\ \overline{\boldsymbol{P}}_U(z,\, z_s) \cdot \left(\boldsymbol{C}_\ell + \frac{1}{2}\boldsymbol{V}_s\right), & z > z_s \end{cases} \tag{9}$$

where $\overline{\boldsymbol{P}}_D(z,\, z_s)$ or $\overline{\boldsymbol{P}}_U(z,\, z_s)$, named as the propagation matrix from z_s to z is specifically (10), shown at the bottom of the page. If $k = \ell$, $\boldsymbol{V}$ is already given by (4) depending on $z > z_s$ or $z < z_s$. Again the calculation of $\boldsymbol{V}$ by (9) using (10) should be backwardly performed.

Once the horizontal components are known, the vertical components of the fields can be written as

$$\begin{cases} E_z = \dfrac{1}{K_{33}}\left(-K_{31}E_x - K_{32}E_y + S_y Z_0 H_x - S_x Z_0 H_y\right) \\ Z_0 H_z = S_x E_y - S_y H_x. \end{cases} \tag{11}$$

Finally, the fields at any point can be numerically obtained by taking inverse Fourier transform of (9) and (11), i.e.,

$$\boldsymbol{F}(x,\, y,\, z) = \frac{\Delta S_x \Delta S_y}{\lambda_0^2} \sum_{n_x=-N_x}^{N_x-1} \sum_{n_y=-N_y}^{N_y-1} \boldsymbol{F}(n_x \Delta S_x,\, n_y \Delta S_y,\, z) \times e^{jk_0(n_x \Delta S_x x + n_y \Delta S_y y)} \tag{12}$$

where $\boldsymbol{F} = [E_x,\, -E_y,\, E_z,\, Z_0 H_x,\, Z_0 H_y,\, Z_0 H_z]^T$, $\lambda_0 = 2\pi/k_0$ is the wavelength in free-space. The computed ranges of the fields in X and Y directions are confined by $\Delta S_x,\, \Delta S_y$, while the resolutions are determined by N_x and N_y. For instance, if $\Delta S_x = \Delta S_y = 1/10$, $N_x = N_y = 20$, then $X_{\max} = Y_{\max} = \pi/(k_0 \Delta S_x) = 5\lambda_0$, while the resolutions are $\Delta X = \Delta Y = X_{\max}/N_x = (1/4)\lambda_0$.

III. Simulations

The formulations outlined above are used to calculated the ELF excitation of the earth-ionosphere waveguide by a dipole lacated in the lower ionosphere, which can be supposed to be produced by HF heating—a possible approach of ELF generation that may be used for communications to submarines. Ionospheric parameters, including the number densities of electron, different molecules, atoms, and ions, are obtained from MSIS-89 and IRI-89 softwares for summer middays. Collision frequencies between different particles are calculated by using [7, eq. (408)] and the dielectric tensor $\overline{\boldsymbol{K}}$ through [8, eq. (4.6.4)]. The geomagnetic strength is taken to be 0.5 Gauss and the conductivity of the ground to be 0.01 S/m.

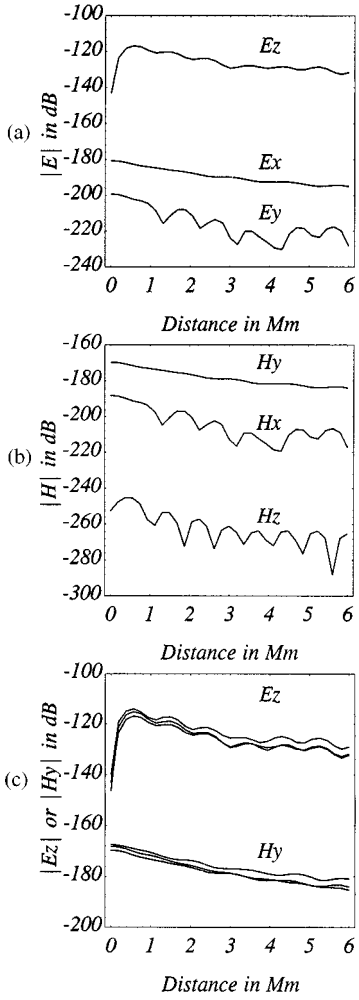

Fig. 2. Field distributions on the ground in X direction. The radiation sources are supposed to be at 76 km above the ground, 30 A · km in strengths, 100 Hz of frequency, and directed in west–east. Note: 0 dB = 1 V/m or 1 A/m. (a) Magnitudes of electric fields, (b) magnetic field strengths, and (c) comparisons of the quasi-TEM waves for the three latitudes.

$$\overline{\boldsymbol{Q}} = \frac{1}{K_{33}} \begin{bmatrix} -K_{31}S_x & K_{32}S_x & S_xS_y & K_{33} - S_x^2 \\ K_{31}S_y & -K_{32}S_y & K_{33} - S_y^2 & S_xS_y \\ K_{23}K_{31} - K_{33}(K_{21} + S_xS_y) & K_{33}\left(K_{22} - S_x^2\right) - K_{23}K_{32} & -K_{23}S_y & K_{23}S_x \\ K_{33}\left(K_{11} - S_y^2\right) - K_{13}K_{31} & K_{13}K_{32} - K_{33}(K_{12} + S_xS_y) & K_{13}S_y & -K_{13}S_x \end{bmatrix} \tag{3}$$

$$\begin{cases} \overline{\boldsymbol{D}} = \overline{\boldsymbol{P}}_\ell(z_s - z_{\ell-1}) \cdot \overline{\boldsymbol{P}}_{\ell-1}(z_{\ell-1} - z_{\ell-2}) \cdots \overline{\boldsymbol{P}}_2(z_2 - z_1) \cdot [\boldsymbol{a}_1\ \boldsymbol{a}_2] \\ \overline{\boldsymbol{U}} = \overline{\boldsymbol{P}}_\ell(z_s - z_\ell) \cdot \overline{\boldsymbol{P}}_{\ell+1}(z_\ell - z_{\ell+1}) \cdots \overline{\boldsymbol{P}}_{N-1}(z_{N-2} - z_{N-1}) \cdot [\boldsymbol{a}_3\ \boldsymbol{a}_4] \end{cases} \tag{6}$$

$$\begin{cases} \overline{\boldsymbol{P}}_D(z,\, z_s) = \overline{\boldsymbol{P}}_k(z - z_k) \cdot \overline{\boldsymbol{P}}_{k+1}(z_k - z_{k+1}) \cdots \overline{\boldsymbol{P}}_{\ell-1}(z_{\ell-2} - z_{\ell-1}) \cdot \overline{\boldsymbol{P}}_\ell(z_{\ell-1} - z_s), & k < \ell \\ \overline{\boldsymbol{P}}_U(z,\, z_s) = \overline{\boldsymbol{P}}_k(z - z_{k-1}) \cdot \overline{\boldsymbol{P}}_{k-1}(z_{k-1} - z_{k-2}) \cdots \overline{\boldsymbol{P}}_{\ell+1}(z_{\ell+1} - z_\ell) \cdot \overline{\boldsymbol{P}}_\ell(z_\ell - z_s), & k > \ell \end{cases} \tag{10}$$

The field distributions on the ground for Beijing area are plotted in Fig. 2(a) and (b). It shows that $|E_z|$ is much larger than $|E_x|$ and $|E_y|$, while $|H_z|$ is much smaller than $|H_x|$ and $|H_y|$. This proves that the fields in the earth-ionosphere waveguide are dominantly transversal, i.e., the so-called quasi-TEM waves. A comparison of the field strengths of $|E_z|$ and $|H_y|$, the principal components of the QTEM waves, for Tromsø, Beijing and Haikou, latitudes north 79°, 40°, and 20°, respectively, is illustrated in Fig. 2(c). Little differences exist for the three regions if the sources are the same in strength, frequency, and height.

REFERENCES

[1] R. Barr, P. Stubbe, M. T. Mietveld, and H. Kopka, "ELF and VLF signals radiated by the 'Polar electrojet antenna': Experimental results," *J. Geophys. Res.*, vol. 91, no. A4, pp. 4451–4459, 1986.

[2] I. Kimura, P. Stubbe, M. T. Rietveld, R. Barr, K. Ishida, Y. Kasahara, S. Yagatani, and I. Nagano, "Collaborative experiments by Akebono satellite, Tromso ionospheric heater, and European incoherent scatter radar," *Radio Sci.*, vol. 29, no. 1, pp. 23–37, 1994.

[3] V. K. Tripathi, C. L. Chang, and K. Papadoloulos, "Excitation of the Earth-ionosphere waveguide by an ELF source in the ionosphere," *Radio Sci.*, vol. 17, no. 5, pp. 1321–1326, 1982.

[4] S. Yagitani, I. Nagano, K. Miyamura, and I. Kimura, "Full wave calculation of ELF/VLF propagation from a dipole source located in the lower ionosphere," *Radio Sci.*, vol. 29, no. 1, pp. 39–54, 1994.

[5] I. Nagano, M. Mambo, and G. Hutatsuishi, "Numerical calculation of electromagnetic waves in an anisotropic multilayered medium," *Radio Sci.*, vol. 10, no. 6, pp. 611–617, 1975.

[6] T. M. Habashy, S. M. Ali, J. A. Kong, and M. D. Grossi, "Dyadic Green's function in a planar stratified, arbitrarily magnetized linear plasma," *Radio Sci.*, vol. 26, no. 3, pp. 701–715, 1991.

[7] H. Rishbeth, *Introduction to Ionospheric Physics*. New York: Academic, 1969.

[8] K. C. Yeh and C. H. Liu, *Theory of Ionospheric Waves*. New York: Academic, 1972.